



HAL
open science

Observation of the compatibility of stimulated Raman histology with pathology workflow and genome sequencing

Barbara Sarri, Romain Appay, Sandro Heuke, Flora Poizat, Florence Franchi, Sébastien Boissonneau, Fabrice Caillol, Henry Dufour, Dominique Figarella-branger, Marc Giovaninni, et al.

► To cite this version:

Barbara Sarri, Romain Appay, Sandro Heuke, Flora Poizat, Florence Franchi, et al.. Observation of the compatibility of stimulated Raman histology with pathology workflow and genome sequencing. *Translational Biophotonics*, 2021, 3 (3), pp.e202000020. 10.1002/tbio.202000020 . hal-03283331

HAL Id: hal-03283331

<https://hal.science/hal-03283331v1>

Submitted on 7 Sep 2021

HAL is a multi-disciplinary open access archive for the deposit and dissemination of scientific research documents, whether they are published or not. The documents may come from teaching and research institutions in France or abroad, or from public or private research centers.


L'archive ouverte pluridisciplinaire **HAL**, est destinée au dépôt et à la diffusion de documents scientifiques de niveau recherche, publiés ou non, émanant des établissements d'enseignement et de recherche français ou étrangers, des laboratoires publics ou privés.



Distributed under a Creative Commons Attribution 4.0 International License

RESEARCH ARTICLE

Observation of the compatibility of stimulated Raman histology with pathology workflow and genome sequencing

Barbara Sarri^{1,2} | Romain Appay^{1,3} | Sandro Heuke¹ | Flora Poizat⁴ |
Florence Franchi⁴ | Sébastien Boissonneau³ | Fabrice Caillol⁴ |
Henry Dufour³ | Dominique Figarella-Branger³ | Marc Giovaninni⁴ |
Hervé Rigneault^{1,2} 

¹Aix Marseille University, CNRS, Centrale Marseille, Institut Fresnel, Marseille, France

²Lightcore Technologies, Cannes, France

³Aix-Marseille University, APHM, CNRS, INP, Inst Neurophysiopathol, CHU Timone, Service d' Anatomie Pathologique et de Neuropathologie, Marseille, France

⁴Institut Paoli-Calmettes, Endoscopy and Gastroenterology Department, Marseille, France

Correspondence

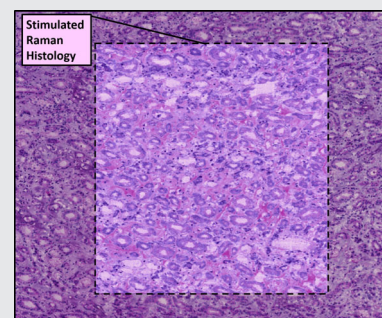
Hervé Rigneault, Aix Marseille University, CNRS, Centrale Marseille, Institut Fresnel, Marseille, France.
Email: herve.rigneault@fresnel.fr

Funding information

Institut Paoli-Calmettes; Aix-Marseille University, Grant/Award Number: A-M-AAP-ID-17-13-170228-15.22-RIGNEAULT; Assistance Publique hôpitaux de Marseille (AP-HM); Canceropôle PACA; Institut National de la Santé et de la Recherche Médicale, Grant/Award Numbers: 18CP128-00, PC201508; Agence Nationale de la Recherche, Grant/Award Numbers: ANR-11-IDEX-0001-02, ANR-10-INSB-04-01, ANR-11-INS, ANR-19-CE19-0019-02; Institut National Du Cancer; Canceropôle Provence-Alpes-Côte d'Azur; Aix-Marseille Université; Centre National de la Recherche Scientifique

Abstract

We show that human samples imaged with stimulated Raman histology (SRH) can be successfully used in a typical pathology workflow including hematoxylin and eosin staining (HE), immunohistochemistry, and genome sequencing. We provide a morphological comparison of SRH images with the gold standard HE and HES (HE and saffron) staining over



three normal tissues from various organs (liver, kidney, and ileum) and two tumoral brain samples (metastatic adenocarcinoma and glioblastoma). Most importantly, we show that a sample imaged with SRH has a comparable microscopic appearance as a control sample (that was not imaged by SRH) including protein expression evaluated by immunohistochemistry as well as similar genetic alterations evaluated by genome sequencing. This suggests that SRH can provide a direct diagnosis without material preparation nor consumption.

KEYWORDS

histology, stimulated Raman histology, stimulated Raman imaging

This is an open access article under the terms of the Creative Commons Attribution License, which permits use, distribution and reproduction in any medium, provided the original work is properly cited.

© 2021 The Authors. *Translational Biophotonics* published by Wiley-VCH GmbH.

1 | INTRODUCTION

Stimulated Raman histology (SRH) is a novel imaging optical technique that has been recently acclaimed to produce histology images that closely resemble standard hematoxylin and eosin (HE) images [1], the latter being used worldwide as the gold standard stain for histological examination of human tissues [2]. Originally developed in the brain imaging context [3, 4], SRH has been extended to the gastro-intestinal tract to produce virtual hematoxylin, eosin, and saffron (HES) images [5, 6]. SRH uses stimulated Raman scattering (SRS) as the main contrast mechanism [7] that provides chemical bond imaging without requiring any labeling or staining [8, 9]. In SRH, both the CH_2 and CH_3 chemical bonds are imaged at the sample plane to provide a “lipid-rich” image and a “protein-rich” image, respectively, from which the difference reveals the cell nuclei, a key feature in tissue microscopic analysis (Figure 1). Subsequent coloring of the obtained

(CH_2) and ($\text{CH}_3\text{-CH}_2$) SRS images using pink and purple look-up tables enables to generate SRH images with striking similarity with HE conventional images [6]. SRS of CH_2 and CH_3 chemical bonds can be also nicely complemented with second-harmonic generation (SHG) imaging that reveals the collagen distribution in tissues [10]. A specific look-up table mimicking the saffron stain can be assigned to this SHG signal to provide images that closely resemble HES conventional images (Figure 1). Throughout this paper, we will refer to SRH using stimulated Raman to generate HE images or its combination with SHG to generate HES images.

Although SRH images have been demonstrated in the brain and in gastric tissues to provide exquisite architectural information, there is no report so far that demonstrates the full compatibility of SRH with the histology pathology workflow that requires immunohistochemistry and genome sequencing. In this paper, we bridge that gap and show, for the first time, that a fresh brain human

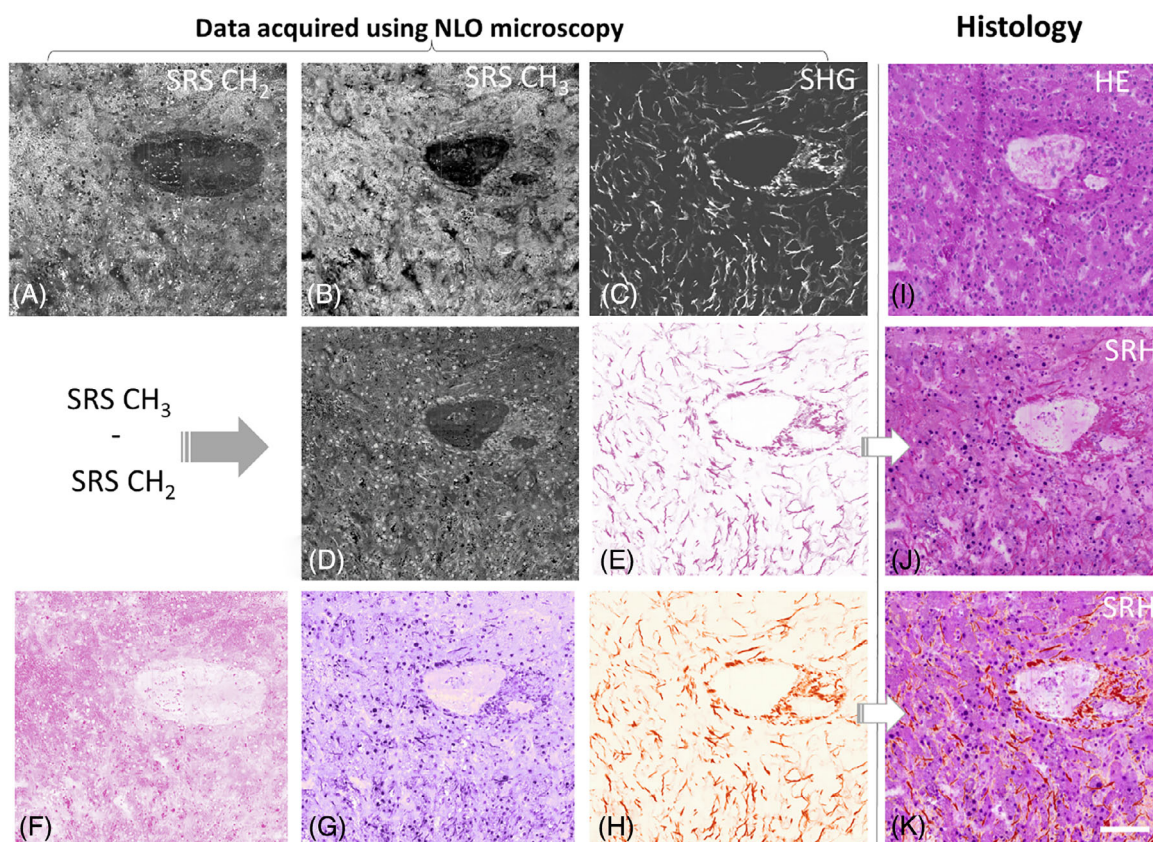


FIGURE 1 Building virtual stained images using stimulated Raman histology (SRH). (A-C). The data are acquired using nonlinear optical microscopy (NLO) via the two SRS channels, (A) and (B) highlighting the lipid (CH_2) and proteins (CH_3) distributions, respectively. (C) SHG channel gives access to the collagen distribution. (D) A simple subtraction (B)-(A) reveals the nuclei distribution. (E-H) Look-up tables (LUTs) are applied to (A-C) to mimic hematoxylin, eosin and saffron (HES) staining: (F) LUT in the pink shades is applied to (A) to copy eosin stain, (G) LUT in the dark purple is applied to (D) to resemble hematoxylin stain. Depending on the desired result (HE vs HES), a LUT in the pink shades (E) or in the orange/brown shades (H)—to virtually reproduce saffron stain—is applied to (C). (J) Combining (E), (F), and (G) allows to produce HE-like image while merging (F-H) enables to get HES-like virtually stained image (K). (I) HE image of the same section for comparison with SRH images (J) and (K). Scale bar 100 μm

sample imaged with SRH can then be successfully used in a typical pathology workflow including HES staining, immunohistochemistry, and genome sequencing, showing the same protein and genomic signature as a control sample (that was not imaged by SRH). We further show morphological comparison of SRH images with the standard HE staining over various human samples including normal and tumor tissues. Frozen sections were first imaged by SRH before being stained with HE to allow direct comparison of the virtually stained SRH images with the routinely used HE over the same samples. We report excellent agreement between the two techniques regardless of the miscellaneous architectures and the diversity of the sample probed.

These results demonstrate further the relevance of SRH as a novel tool for microscopic analysis, being able to perform stain-free histological examinations of precious excised tissues, without material consumption, as enabling subsequent immunohistochemistry and genome sequencing, on the same sample.

2 | MATERIALS AND METHODS

2.1 | Human samples

Freshly excised human samples from three normal tissues of various organs (liver, kidney, and ileum) as well as two central nervous system tumors (one glioblastoma and one metastatic adenocarcinoma) obtained from five different patients were embedded in optical cutting temperature compound (OCT) and frozen in a container of liquid nitrogen-cooled isopentane, a procedure reducing freezing artifacts. Frozen sections (8-10 μm thick) of these samples were obtained using a standard cryostat microtome. The sections were then deposited onto a slide and imaged with SRS and SHG without further preparation. One-to-one comparison, that is, comparison of the same sample between the SRH image and the standard HE stained one, was performed by HE staining of the SRH imaged slide.

In addition, SRH images were also performed on a cubic millimeter freshly excised brain tumor sample from a sixth patient placed between two coverslips without further preparation. After SRH imaging, this bulk sample was included in the full conventional pathology workflow including formalin fixation, paraffin embedding, HES staining, immunohistochemistry, and genome sequencing. Additional analyses were performed within the Assistance Publique-Hôpitaux de Marseille (AP-HM) pathology department with validated protocols used for routine diagnosis. Quickly, automated immunohistochemistry was performed with 3.5- μm -thick formalin-

fixed paraffin-embedded (FFPE) sections with an avidin-biotin-peroxidase complex on Benchmark XT (Ventana Medical System Inc., Tucson AZ) using the Ventana Kit including DAB reagent to search for the expression of OLIG2 (Diagomics, clone EP112, 1/100 dilution), GFAP (DAKO, clone GF2, 1/200 dilution), IDH1 R132H (Dianova, clone H09, 1/100 dilution) and ATRX (BioSB, clone BSB-108, 1/200 dilution). Regarding genome sequencing, tumor DNA was extracted from $4 \times 5\text{-}\mu\text{m}$ thick sections of FFPE tissue samples using the Maxwell RSC DNA FFPE Kit (Promega Corporation), and the Ion S5 XL next-generation sequencing system (Thermo Fisher Scientific) was used to perform targeted sequencing of the 18 following genes: *AKT1*, *ATRX*, *BRAF*, *CDKN2A*, *CIC*, *EGFR*, *FGFR1*, *H3F3A*, *HIST1H3B*, *IDH1*, *IDH2*, *NOTCH1*, *PIK3CA*, *PIK3R1*, *PTEN*, *PTPN11*, *TERT*, *TP53*.

2.2 | Nonlinear imaging (NLO microscopy)

To accomplish SRH, SRS images of both lipids and proteins, as well as SHG images of collagen, were acquired simultaneously. The details of the laser sources and microscope have been described in Reference [11]. Briefly, an ytterbium (Yb) fiber laser (2 ps pulse duration, repetition rate 80 MHz) (Emerald Engine APE) emitting at 1031 nm is used as the Stokes beam on the one hand and is frequency doubled (515 nm) on the second hand to pump two optical parametric oscillators (OPO₁ and OPO₂ Emerald APE). This generates two pump beams whose wavelengths are settled at 797.3 nm (OPO₁) and 792.2 nm (OPO₂). This way, both molecular vibration modes, of CH₂ (2845 cm⁻¹) and CH₃ (2930 cm⁻¹), are addressed simultaneously when the OPO beams are recombined with the 1031 nm Stokes beam (recombination with dichroic mirrors TBP01-900/11 Semrock and DMSP900R Thorlabs). SRS detection is performed simultaneously using these three beams by modulating OPO₁ at RF frequency f_1 ($f_1 = 14.34$ MHz) and OPO₂ at RF frequency f_2 ($f_2 = 14.74$ MHz), by acousto-optic modulators (AA Optoelectronic MT200-AO). Delay lines allow to reach the temporal overlap of the 1031 nm with OPO₁ and OPO₂ pulses while other mirrors direct the beams into a custom build scanning microscope [11]. A custom made software allows to control both the microscope and the OPOs [12]. The beams are focused onto the sample using an objective (Nikon, CFI APO 40x WI Lambda S with NA = 1.15, water) while a condenser (Nikon, c-c condensor Achromat/Aplanat, NA = 1.4) collects the light in the forward direction. Spectral filtering (SP980, Semrock) is applied before the Stokes beam is detected by

a photodiode (APE, LIA photodiode). The latter is connected to a dual-channel lock-in-amplifier (HF2LI Zurich Instrument) which demodulates the signal at f_1 and f_2 . This allows to record the two CH_2 (2845 cm^{-1}) and CH_3 (2930 cm^{-1}) SRS signals simultaneously at each pixel. In addition, the SHG signal is detected in the epi (backward) direction, simultaneously to the SRS CH_2 and CH_3 signals, using a bandpass filter (420/40) and a photomultiplier tube (Perkin Elmer, MP-943). Millimeter sized images were achieved by stitching next to each other smaller galvo-scanned images (field of view $100\text{ }\mu\text{m} \times 100\text{ }\mu\text{m}$ for cryogenic slides and $200\text{ }\mu\text{m} \times 200\text{ }\mu\text{m}$ for bulk biopsies). Laser powers used at the sample were 18 to 20 mW for each beam for thin cryogenic slides and 30 mW (for each beam) for bulk biopsies. The pixel dwell time was set to 40 μs and the individual images were averaged over three consecutive accumulations. Using a pixel step size of 500 nm, 25 minutes were required to acquire and stitch a $1\text{ mm} \times 1\text{ mm}$ image.

2.3 | HE and SRH images

HE images were obtained using Hamamatsu's virtual slide scanner Nanosizer 2.0-HT with the NDP.view2 or Calopix viewing software. Virtually stained SRH images were built using a Matlab-based custom program described in Reference [6]. Figure 1 summarizes how data are processed for a liver frozen section first imaged by SRS and SHG (Figure 1A-C), then stained with HE (Figure 1I). It also exemplifies how virtual HE (Figure 1J) and virtual HES (Figure 1K) can be obtained. As detailed in Reference [6], three images are used as inputs to build the virtually stained SRH image: (1) The SRS image at 2845 cm^{-1} —which provides the lipid distribution (CH_2 bond—Figure 1A), (2) the SRS image built from the subtraction of the SRS image at 2930 cm^{-1} , providing mainly the protein distribution (CH_3 bond) (Figure 1B), minus the SRS CH_2 image (2845 cm^{-1}). This CH_3 - CH_2 image allows to reveal the cell nuclei as shown in (Figure 1D). Finally, the SHG signal (3) showing the collagen (Figure 1C) is also needed. Homemade look-up tables (LUTs) in the pink and dark purple shades are then, respectively, applied to (1) (CH_2 — Figure 1F) and (2) (CH_3 - CH_2 —Figure 1G) to mimic eosin and hematoxylin stains. Depending on the desired result (HE vs HES), it is possible to whether apply a LUT in the pink shades (3) (collagen Figure 1E) or in the orange/brown shades which reproduces saffron stain (collagen—Figure 1H). Combining Figure 1E (collagen), Figure 1F (lipid) and Figure 1E (nuclei) allows to produce a stain-free, HE-like, SRH image while merging Figure 1F-H enables to get, HES-like, SRH image (Figure 1K). The

former is useful for one-to-one SRH/HE comparison (see Figure 1J, I), while the latter is useful for one-to-one SRH/HES comparison where the collagen fibrils network is more clearly visible (Figure 1K). Standard HE image of the same section is also given for comparison (Figure 1).

3 | RESULTS AND DISCUSSION

3.1 | SRH analysis of liver, kidney, and ileum samples

We first concentrated on visceral organs such as liver, kidney, and ileum. Figure 2 displays mm^2 images of human frozen sections first acquired by SRH, then stained in HE of: liver Figure 2A-C, kidney Figure 2D-F and ileum Figure 2G-I. In figures Figure 2A, D, and G, SRH images are directly superimposed into the corresponding HE images from the same sample. This allows to appreciate the general sample architecture and the SRH/HE comparison at low magnification. Smaller portions of the SRH images (black frames in Figure 2A, D, and G) are additionally given in Figure 2B, E, and H to compare cytonuclear features at higher magnification with their HE counterparts (Figure 2C, F, and I) and to visually assess for quasi-perfect matching between SRH and HE.

As one can evaluate the general architecture of the liver is readily recognizable in Figure 2A. The faint transition between the SRH image (in the middle) and the HE (all around) asserts for similar histological coloring with both techniques. To appreciate further both the quality and the quasi-perfect matching between SRH and HE at the cytosolic level, a one-to-one comparison centered on the portal tract is provided at enhanced magnification (Figure 2B-C). The constitutive elements of the portal tract can be identified with both techniques. This includes the portal vein (X), the hepatic artery (\blacktriangle), the bile duct (Δ), and a lymphatic vessel (*). This portal tract lies in a network of connective tissue (dark pink), better highlighted within the SRH image mimicking the HES stains (illustrated in Figure 1K) compared to both the SRH image mimicking the HE stains (Figure 2B) or rapid HE (Figure 2C). The portal tract is also surrounded by numerous hepatocytes (gray arrow) constituting the liver parenchyma. In Figure 2B,C, the characteristic heterogeneous size of the hepatocyte nuclei, related to the polyploid capacity of these cells, can be observed.

Performing one-to-one SRH/HE comparison on kidney Figure 2D-F and ileum Figure 2G-I frozen sections led to the same agreement. The general architecture of the tissues appears comparable with the two approaches at both low magnification (Figure 2D and G) and high magnification (Figure 2E-F and H-I). For didactic purpose, the

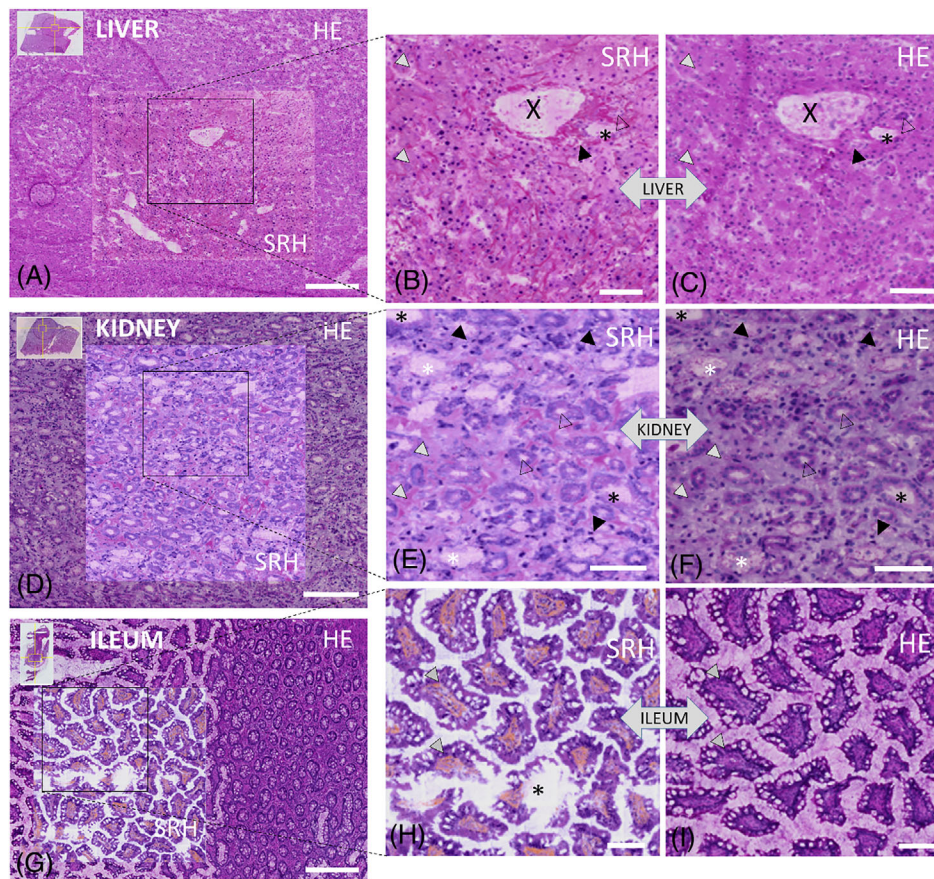


FIGURE 2 One-to-one comparison between stimulated Raman histology (SRH) and standard hematoxylin and eosin (HE) of cryogenic section of healthy tissues: (A-C) liver, (D-F) kidney, and (G-I) ileum. (A) SRH image of liver encapsulated within a larger zone of the same HE section; one-to-one SRH/HE comparison (B,C) is presented on a limited region of interest ROI (black-framed region in A). (B) SRH image zoomed around the portal triad, (C) HE of the same region. From (B) and (C), all tissue characteristics from the portal triad can be identified: the portal vein (X), a lymphatic vessel (*), the hepatic artery (▲), and the bile duct (Δ). Hepatocytes (gray triangles) are numerous and present all around the portal triad. (D) SRH image from the deep cortical region of a kidney encapsulated within a larger region of the same HE section; one-to-one SRH/HE comparison is provided at higher magnification (ROI = black frame in D). Features from the deep cortical region can be seen: collecting tubules, proximal convoluted tubules (white asterisk), distal convoluted tubule (Δ), collecting duct tubes (*), intercalated cells (▲), collagen fibers (gray arrows). (E) SRH (F) HE of the same region. (G) SRH image of ileum section encapsulated within a wider zone of the HE section; one-to-one SRH/HE comparison is provided at higher magnification (ROI = black frame in G). (H) SRH (I) HE of the same region. (A), (G) scale bar = 300 μm; (d) scale bar = 250 μm; others scale bar = 100 μm

collagen network was colored in darker pink shades compared to the cytosolic content on the kidney SRH image (Figure 2E) while it was implemented in saffron-like colors in the ileum SRH image (Figure 2H) to allow distinguishing SRH and HE in Figure 2G. In Figure 2D-F, a kidney section from the medulla region is presented. With both modalities SRH and HE, tubules and collecting duct constituting the medulla region are recognizable (*). Cells intercalated within the connective tissue network are also present (▲) as well as collagen fibers (gray arrows). These are slightly more visible on the SRH image (Figure 2E). Figure 2G-I focuses on the mucosa region of the ileum. The characteristic ileum histology associating crypts and villi is readily recognizable both in SRH and HE. Crypts of

Lieberkühn are observable on the right side of Figure 2G while the mucosa villi pointing toward the periphery (located on the left side) are presented in Figure 2H,I. SRH/HE matching is close to perfect: all vacuoles, lumen, and nuclei appear comparable while the collagen fibrils colored in orange/brown in SRH allow differentiating between SRH and HE (Figure 2G). If the sample seems locally altered (*) in Figure 2H (compared to HE Figure 2I), this is because SRH provides optical sectioning, and the sample section is not completely flat: this region lies away from the SRH imaging plane. These results demonstrate the potential of SRH to both generate detailed histological images for visceral tissue architectures, and to reveal physiologically relevant features, with comparable quality as standard HE.

3.2 | SRH imaging of central nervous system tumor samples

To assess SRH-imaging on the central nervous system (CNS), SRH imaging, and HE staining were conducted on the same brain tumors frozen sections. We concentrate on a metastatic adenocarcinoma (Figure 3A-C) and a glioblastoma (Figure 3D-F). SRH images (Figure 3A,D) are integrated within a wider HE view of the samples. In both cases, one-to-one comparison showed equivalent content. On the first sample (Figure 3A-C), all features necessary to assert for brain colon adenocarcinoma are identically present on both the SRH (Figure 3B) image and the HE (Figure 3C) one. The general tissue architecture is greatly altered on both images as revealed by the presence of numerous moderately differentiated glandular structures (▲) associated with a dense collagenous stroma (gray arrow). High magnification showed on both SRH and HE the presence of atypical cells characterized by basally oriented

pleomorphic nuclei. The second sample (Figure 3D-F), although pre-necrotic, demonstrates that SRH allows to highlight the same features as standard HE to diagnose a brain glioblastoma. Indeed, Figure 3B,C demonstrated a diffuse infiltrative growth pattern of altered glial cells with atypical nuclei embedded in a matrix of pre-necrotic neuropil.

3.3 | SRH compatibility with the conventional pathology workflow: immunochemistry and gene sequencing

Central nervous system (CNS) tumors encompass a large number of heterogeneous neoplasms with different outcomes and treatment strategies [13–15]. In order to perform a correct sampling of a tumor, the neurosurgeon may request an intraoperative pathologist consultation to assess the quality of the collected sample. However, this preliminary pathological examination inevitably requires

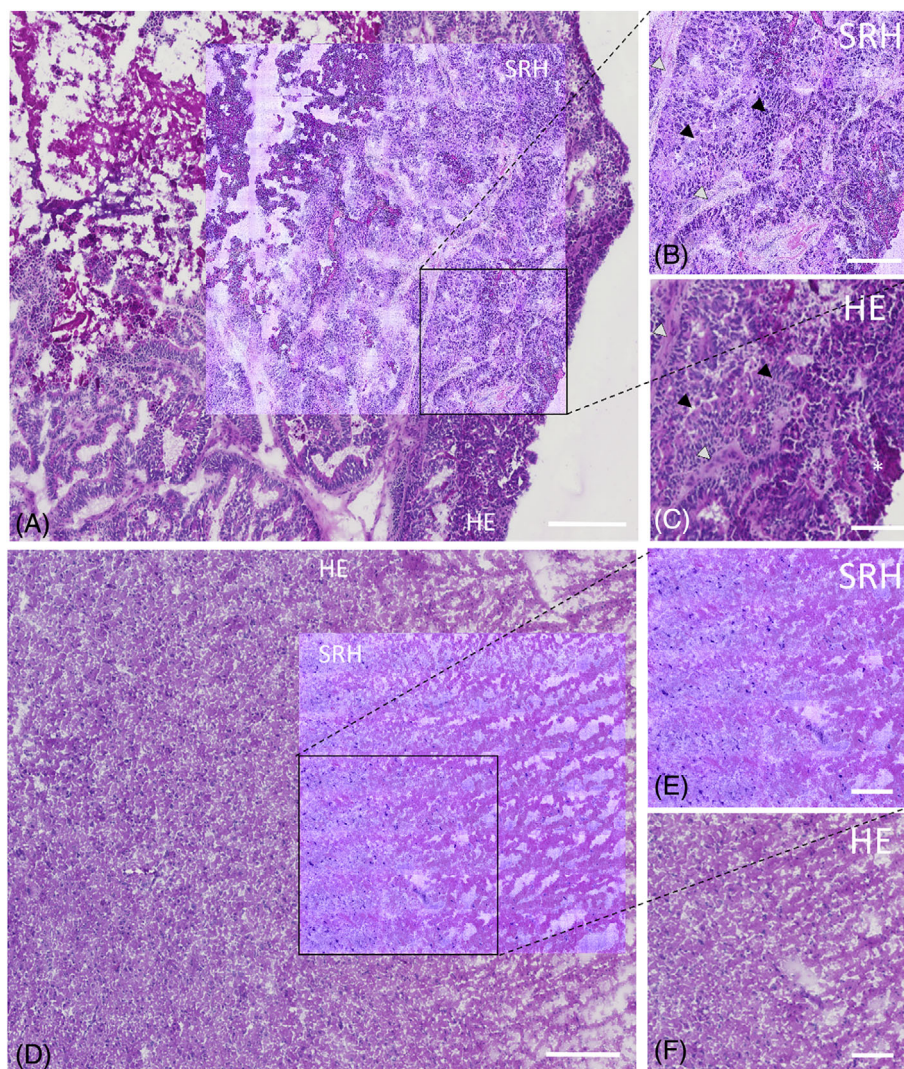


FIGURE 3 One-to-one comparison between stimulated Raman histology (SRH) and standard hematoxylin and eosin (HE) of brain cryogenic sections: (A) SRH image of a brain colon adenocarcinoma inserted into a larger area of the HE section; higher magnification ([B] SRH and [C] HE) is provided for a region of interest (black framed in [A]). (D) SRH image of a brain glioblastoma inserted into a larger area of the HE section; higher magnification ([E] SRH and [F] HE) is provided for a region of interest (black framed in [D]). (A,D) Scale bar = 250 μm , (B,E) Scale bar = 50 μm , (C,F) Scale bar = 100 μm

the consumption of a small and valuable brain material. Indeed, in the today's "molecular diagnostic era," more and more additional evaluations, including immunohistochemistry and genome sequencing, become mandatory. In the case of brain stereotaxic biopsies, they have to be performed on a very limited tissue sample ($\sim\text{mm}^3$). The ability to perform SRH imaging directly on a freshly excised brain biopsy, still keeping the same sample available for further immunohistochemistry and gene sequencing investigation would be a breakthrough with immediate benefit for the patient.

In the purpose of addressing the potential of SRH for intraoperative pathological diagnosis without tissue depletion nor alteration, a freshly excised CNS tumor sample imaged with SRH was included into a conventional pathology workflow including HE staining, immunohistochemistry, and genome sequencing. The results were compared to the one obtained on the routinely processed sample (ie, not subjected to SRH analysis). Results are summarized in Figure 4. A freshly excised brain biopsy was directly deposited into a 500 μm spacer between coverslips without further preparation (Figure 4A) and imaged with SRH (Figure 4B) at ~ 200 μm depth. After the SRH imaging, the sample has been fixed in formalin, embedded in paraffin, and stained with H&E (Figure 4C). The cancerous nature of the sample could be readily assessed by SRH with the visualization of the diffuse proliferation of pleomorphic glial cells

with nuclear atypia asserting for high-grade glioma (Figure 4B). Notably, the appearance was comparable to those observed on the HE routinely processed sample (Figure 4C,D). Another part of the sample (the control sample not imaged with SRH) was directly fixed in formalin and embedded in paraffin to undergo standard HE staining (Figure 4D).

Next, the SRH imaged sample and the non-SRH imaged sample allow into the same immunohistochemistry and gene sequencing processes. As illustrated in Figure 4E (sample imaged with SRH) and Figure 4F (control sample), the immunohistochemical observations on both samples were similar. The expression of the glial fibrillary acidic protein (GFAP) and of the oligodendrocyte transcription factor (OLIG2) attested for the glial nature of the tumor cells. Both samples did not demonstrate the most frequent mutation in the gene encoding isocitrate dehydrogenase 1 (IDH1) as demonstrated by the absence of immunostaining with the antibody targeting the IDH1 R132H mutant protein. Finally, the Alpha Thalassemia/Mental Retardation Syndrome X-Linked (ATRX) nuclear expression was retained in both cases suggesting the absence of ATRX gene alteration.

Genome sequencing performed on both samples demonstrated similar results: in both cases a mutation in the *TERT* promoter region (NM_198253:2:c.1-146C>T) without alteration of the other sequenced genes. Since the

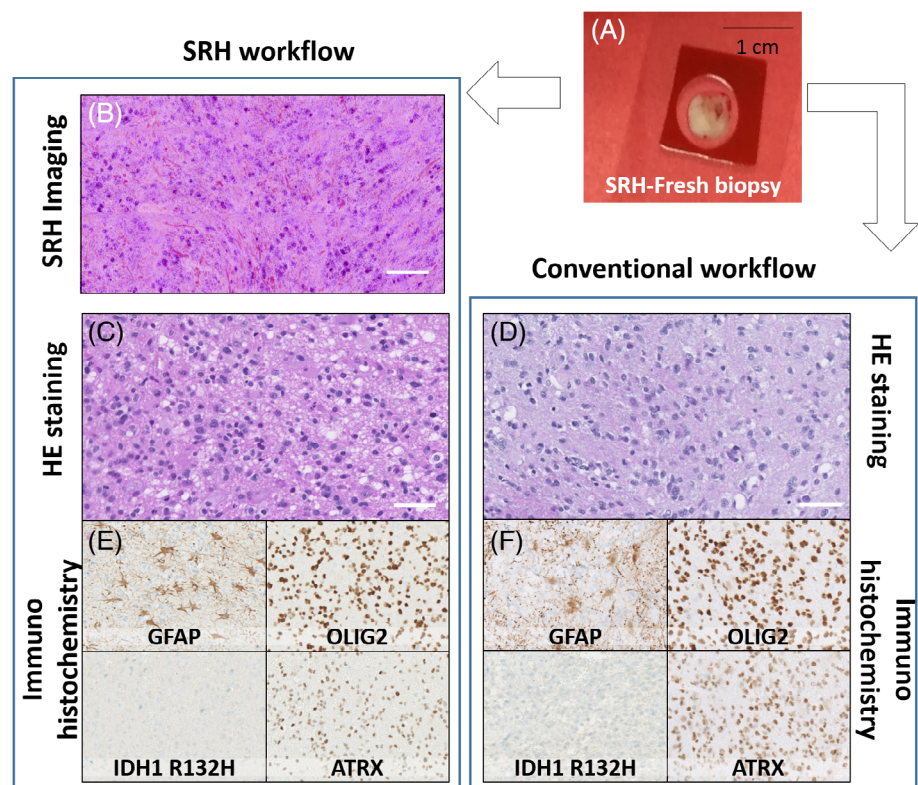


FIGURE 4 Histology workflows including SRH. A fresh brain biopsy sample (A) enters two workflows: the "SRH workflow" (left) includes SRH imaging (B), HE staining (C), and immunohistochemistry (E); while the second "conventional workflow" includes HE staining (D), and immunohistochemistry (F). Full immunohistochemistry analysis performed in both workflows includes anti-GFAP, OLIG2, IDH1 R132H, and ATRX antibodies

World Health Organization (WHO) CNS tumor classification [13], the diagnosis of several tumors requires the characterization of potential molecular abnormalities to establish an “integrated” morphological, and molecular diagnosis (eg, glioblastoma IDH-mutant vs glioblastoma IDH-wildtype). In both cases, a similar integrated diagnosis of glioblastoma, IDH-wildtype could be assessed. This preliminary result suggests that SRH analysis does not introduce sample alteration from microscopic, immunohistochemical nor molecular point of views. This “proof-of-principle” study needs now to be completed by an extended investigation including a statistically relevant number of samples, potentially on several pathological cases and organs.

4 | CONCLUSION

In this study, we showed one-to-one comparison images of SRH with standard HE-stained images for different organs (liver, kidney, and ileum) with diversified parenchymal architecture as well as for different type of CNS neoplasms. We showed that SRH constitutes a method with potential to perform a histopathological examination of sliced or freshly excised human samples with microscopic features comparable to those observed with conventional HE staining. In addition, we reported for the first time that a fresh brain tissue biopsy imaged with SRH can successfully enter into the conventional immunohistochemistry and genome sequencing processes, suggesting the absence of SRH-induced sample alterations. As the screening of relevant biomarkers becomes more and more important in the diagnosis process and is increasingly sample consuming, the incorporation of SRH into the histology workflow to generate “HE-like” images is awaited provide direct diagnosis without material preparation nor consumption. This would represent a major advance for both surgeon and pathologists with direct benefit for the patients.

ACKNOWLEDGMENTS

This study is supported by Assistance Publique hôpitaux de Marseille (AP-HM), Institut Paoli-Calmettes (IPC), Centre National de la Recherche Scientifique; Aix-Marseille Université (A-M-AAP-ID-17-13-170228-15.22-RIGNEAULT); A*Midex (ANR-11-IDEX-0001-02); Canceropôle Provence-Alpes-Côte d’Azur; Institut National Du Cancer; Région Sud; Agence Nationale de la Recherche (ANR-10-INSB-04-01, ANR-11-INSB-0006, ANR-19-CE19-0019-02); Institut National de la Santé et de la Recherche Médicale (18CP128-00, PC201508).

CONFLICT OF INTEREST

The authors declare no conflict of interest.

AUTHOR CONTRIBUTIONS

B.S., R.A., S.H. performed the SRS imaging measurements. B.S, R.A. performed the SRH virtual coloring. R.A., D.F-B, F.P., F.F performed the histology HE, immunohistochemistry, and gene sequencing. S.B, H.D., F.C., M.G. collected the samples. M.G., H.D., D.F-B, H.R. designed the research. B. S., R. A., H. R. wrote the manuscript with input from all co-authors.

DATA AVAILABILITY STATEMENT

The data that support the findings of this study are available from the corresponding author upon reasonable request.

ORCID

Hervé Rigneault  <https://orcid.org/0000-0001-6007-0631>

REFERENCES

- [1] D. A. Orringer, B. Pandian, Y. S. Niknafs, T. C. Hollon, J. Boyle, S. Lewis, M. Garrard, S. L. Hervey-Jumper, H. J. L. Garton, C. O. Maher, J. A. Heth, O. Sagher, D. A. Wilkinson, M. Snuderl, S. Venneti, S. H. Ramkissoon, K. A. McFadden, A. Fisher-Hubbard, A. P. Lieberman, T. D. Johnson, X. S. Xie, J. K. Trautman, C. W. Freudiger, S. Camelo-Piragua *Nature, Biomed Eng* **2017**, *1*, 27.
- [2] J. Rosai Lab, *Invest.* **2007**, *87*, 403.
- [3] T. C. Hollon, B. Pandian, A. R. Adapa, E. Urias, A. V. Save, S. S. S. Khalsa, D. G. Eichberg, R. S. D’Amico, Z. U. Farooq, S. Lewis, P. D. Petridis, T. Marie, A. H. Shah, H. J. L. Garton, C. O. Maher, J. A. Heth, E. L. McKean, S. E. Sullivan, S. L. Hervey-Jumper, P. G. Patil, B. G. Thompson, O. Sagher, G. M. McKhann, R. J. Komotar, M. E. Ivan, M. Snuderl, M. L. Otten, T. D. Johnson, M. B. Sisti, J. N. Bruce, K. M. Muraszko, J. Trautman, C. W. Freudiger, P. Canoll, H. Lee, S. Camelo-Piragua, D. A. Orringer, *Nat Med.* **2020**, *26*, 52.
- [4] M. Ji, S. Lewis, S. Camelo-Piragua, S. H. Ramkissoon, M. Snuderl, S. Venneti, A. Fisher-Hubbard, M. Garrard, D. Fu, A. C. Wang, J. A. Heth, C. O. Maher, N. Sanai, T. D. Johnson, C. W. Freudiger, O. Sagher, X. S. Xie, D. A. Orringer, *Sci Trans Med* **2015**, *7*, 309ra163.
- [5] B. Sarri, R. Canonge, X. Audier, E. Simon, J. Wojak, F. Caillol, C. Cador, D. Marguet, F. Poizat, M. Giovannini, H. Rigneault, *Sci Rep* **2019**, *9*, 10052.
- [6] B. Sarri, F. Poizat, S. Heuke, J. Wojak, F. Franchi, F. Caillol, M. Giovannini, H. Rigneault, *Biomed. Opt. Express.* **2019**, *10*, 5378.
- [7] H. Rigneault, P. Berto, *APL Photonics.* **2018**, *3*, 091101.
- [8] C. W. Freudiger, W. Min, B. G. Saar, S. Lu, G. R. Holtom, C. He, J. C. Tsai, J. X. Kang, X. S. Xie, *Science.* **2008**, *322*, 1857.
- [9] P. Nandakumar, A. Kovalev, A. Volkmer New, *J. Phys.* **2009**, *11*, 033026.
- [10] W. R. Zipfel, R. M. Williams, R. Christie, A. Y. Nikitin, B. T. Hyman, W. W. Webb, *Proc Natl Acad Sci U S A.* **2003**, *100*, 7075.

- [11] S. Brustlein, P. Ferrand, N. Walther, S. Brasselet, C. Billaudeau, D. Marguet, H. Rigneault, *J Biomed Opt.* **2011**, *16*, 021106.
- [12] P. Ferrand, *Comput Phys Commun.* **2015**, *192*, 342.
- [13] D. N. Louis, A. Perry, G. Reifenberger, A. von Deimling, D. Figarella-Branger, W. K. Cavenee, H. Ohgaki, O. D. Wiestler, P. Kleihues, D. W. Ellison, *Acta Neuropathologica.* **2016**, *131*, 803.
- [14] H. Takei, E. Rouah, *Brain Tumor Pathol* **2016**, *33*, 1.
- [15] K. A. McNeill, *Neurolog Clin* **2016**, *34*, 981.

How to cite this article: B. Sarri, R. Appay, S. Heuke, F. Poizat, F. Franchi, S. Boissonneau, F. Caillol, H. Dufour, D. Figarella-Branger, M. Giovaninni, H. Rigneault, *Translational Biophotonics* **2021**, *3*(3), e202000020. <https://doi.org/10.1002/tbio.202000020>